An improved technique for computing permeability from NMR measurements in mudstones

Hugh Daigle[1] and Brandon Dugan[1]

[1]   We develop a technique for extending nuclear magnetic resonance (NMR) permeability estimation to clay-rich sediments. Our technique builds on the Schlumberger-Doll Research (SDR) equation by using porosity, grain size, specific surface, and magnetic susceptibility data to yield more accurate permeability estimation in mudstones with large pore surface areas and complex mineralogies. Based on measurements of natural sediments as well as resedimented laboratory mixtures of silica, bentonite, and kaolinite powders, we find that our method predicts permeability values that match measured values over four orders of magnitude and among lithologies that vary widely in grain size, mineralogy, and surface area. Our results show that the relationship between NMR data and permeability is a function of mineralogy and grain geometry, and that permeability predictions in clay-rich sediments can be improved with insights regarding the nature of the pore system made by the Kozeny theory. This technique extends the utility of NMR measurements beyond typical reservoir-quality rocks to a wide range of lithologies.

Citation: Daigle, H., and B. Dugan (2011), An improved technique for computing permeability from NMR measurements in mudstones, *J. Geophys. Res.*, *116*, B08101, doi:10.1029/2011JB008353.

1. Introduction

[2]   Knowledge of subsurface permeability is central to many fluid flow problems, including basin-scale modeling, reservoir engineering, aquifer drawdown calculations, wellbore stability, and contaminant transport modeling. In situ measurements of permeability in fine-grained sediments are time consuming and costly to perform, so permeability is often estimated from other sediment properties such as porosity [e.g., *Neuzil*, 1994], specific surface area [*Kozeny*, 1927], grain geometry [*Schwartz and Banavar*, 1989], pore shape [*Yang and Aplin*, 1998], or grain size [*Yang and Aplin*, 2010]. These methods require detailed laboratory measurements of physical samples, and if such information is unavailable accurate permeability estimation may not be possible.

[3]   Nuclear magnetic resonance (NMR) log data are frequently used for permeability estimation in hydrocarbon reservoirs [*Kenyon et al.*, 1995; *Alvarado et al.*, 2003]. This technique allows permeability calculation from wireline log data or logging-while-drilling (LWD) data, eliminating the need for physical samples. *Kenyon et al.* [1988] showed that NMR hydrogen relaxation time data are correlated with permeability, and used measurements of sandstone permeability, porosity, and NMR relaxation times to derive the semiempirical Schlumberger-Doll Research (SDR) equation:

$$k = A\varphi^4 T_{2LM}^2, \tag{1}$$

where k is permeability [m^2], φ is fractional porosity [m^3 m^{-3}], T_{2LM} is the geometric mean of the transverse relaxation time (T_2) distribution [s], and A [m^2 s^{-2}] is an empirical coefficient. Accurate permeability estimation requires calibration with core measurements to constrain values of A; typical values used in petrophysical log analysis are 4×10^{-9} m^2 s^{-2} in sandstones and 1×10^{-10} m^2 s^{-2} in carbonates [*Kenyon et al.*, 1995; *Alvarado et al.*, 2003]. These values are based on laboratory measurements of reservoir-quality rocks (permeability $> 10^{-15}$ m^2). However, A can vary by as much as 2 orders of magnitude from sandstones to mudstones [*Daigle and Dugan*, 2009]. Constraining how A varies with lithology is integral to extending the applicability of equation (1) beyond conventional reservoir-quality rocks to fine-grained sediments which typically make up a large portion of sedimentary sequences.

[4]   Equation (1) relates the permeability of a porous medium to its T_2 distribution. In water-saturated sediments, T_2 is proportional to the ratio of pore volume to pore surface area [*Kleinberg*, 1999]. On the basis of this proportionality, the SDR equation is often compared to Kozeny permeability models [*Kozeny*, 1927; *Carman*, 1937], which relate permeability to internal surface area or the ratio of pore volume to pore surface area. Kozeny permeability models assume that flow occurs in nonintersecting tubular pores that need not be straight or of uniform cross-sectional shape [*Bear*, 1972; *Scheidegger*, 1974]. Such models succeed at predicting permeability in relatively homogeneous, ordered, porous media such as sands [e.g., *Panda and Lake*, 1994; *Wong*, 2003] and idealized pore systems whose fractal geometries are well constrained [e.g., *Costa*, 2006; *Xu and Yu*, 2008]. However, permeability predictions in porous media with more complicated pore networks, like natural

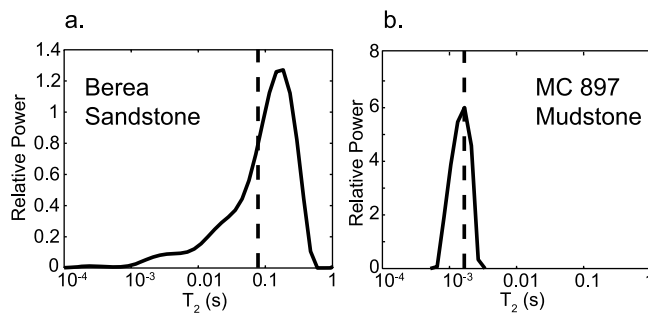[1]Department of Earth Science, Rice University, Houston, Texas, USA.

Figure 1. Example T_2 distributions for (a) Berea sandstone and (b) a mudstone from Mississippi Canyon Block in the northern Gulf of Mexico (MC 897). T_{2LM} in each plot is marked by a dashed vertical line. Berea sandstone has $T_{2LM} = 0.0842$ s and $k = 5.68 \times 10^{-14}$ m^2, and the MC 897 mudstone has $T_{2LM} = 0.00146$ s and $k = 5.98 \times 10^{-18}$ m^2; the T_2 distribution in the lower-permeability MC897 mudstone is shifted to shorter T_2 values. The lower power values for Berea sandstone are due to its lower porosity.

mudstones [*Zhang and Knackstedt*, 1995; *Paterson et al.*, 1996], require modifications to the Kozeny model to account for the complex pore geometry and large internal surface area characteristic of clay-rich sediment [e.g., *Yang and Aplin*, 1998; *Yang and Aplin*, 2007]. By establishing a representative physical model to quantify how A responds to pore geometry parameters like tortuosity and surface area, we can extend the utility of the SDR equation to fine-grained, clay-rich sediments.

[5] Here we present a technique to modify the SDR equation to allow for accurate estimation of permeability in fine-grained sediments. This technique is based on the similarities of the SDR equation [*Kenyon et al.*, 1988] and Kozeny equation [*Kozeny*, 1927], both of which relate permeability to pore geometry and surface area. We modify the parameter A in the SDR equation to account for the complicated pore geometry often exhibited by clay-rich sediment. To quantify lithological variation of A, we compared measurements of permeability, T_{2LM}, porosity, specific surface, grain size, and magnetic susceptibility of natural mudstones and resedimented laboratory mixtures of silica, bentonite, and kaolin powders. We found that A can be computed from magnetic susceptibility, grain size, porosity, and specific surface, and that the relationship between these parameters and A is unique for each sample suite due to differences in mineralogy and grain geometry. Our results highlight the Kozeny nature of the SDR equation, and strengthen the capabilities of NMR data in predicting subsurface permeability in fine-grained sediments of known composition. This extends the utility of NMR measurements for permeability prediction by integration with other sediment properties that may be easily and quickly measured.

2. Background

2.1. NMR Permeability

[6] Borehole NMR tools function by aligning the spin axes of hydrogen nuclei in pore fluid with a large permanent magnet, and then emitting a pulsed magnetic field oriented

perpendicular to the field of the permanent magnet. The hydrogen nuclei precess in the presence of the pulsed field; the precession is initially in phase, but eventually dephases due to inhomogeneities in the field of the permanent magnet. To counteract this, another pulsed field is emitted by the tool oriented opposite to the field of the permanent magnet. This causes the hydrogen nuclei to precess in phase with each other once more, and to emit a radio frequency electromagnetic pulse which is detected by the tool. Eventually fewer and fewer of the hydrogen nuclei can be drawn back in phase with each other, so the amplitude of the electromagnetic pulse decreases as the measurement sequence proceeds. This amplitude decrease follows an exponential decay:

$$C(t) = C_0 e^{\frac{-t}{T_2}}, \tag{2}$$

where C_0 and $C(t)$ are the initial and instantaneous amplitudes, t is time [s], and T_2 is the transverse relaxation time [s] [*Kleinberg*, 1999].

[7] In a water-saturated porous medium, the dominant mechanism for causing irreversible precession dephasing is interactions with paramagnetic ions on pore walls such as Fe^{3+} or Mn^{2+}. It can be shown that T_2 can be approximated as [*Kleinberg*, 1999]

$$T_2 \approx \frac{1}{\rho_2} \frac{V}{S}, \tag{3}$$

where V is pore volume [m^3], S is pore surface area [m^2], and ρ_2 is the transverse surface relaxivity [m s^{-1}]. ρ_2 is an intrinsic property of the minerals forming the pore walls and is a function of paramagnetic ion concentration on the mineral surfaces. Since porous media typically have a range of pore sizes and shapes, they are characterized by a T_2 distribution (Figure 1). The geometric mean of the T_2 distribution, T_{2LM}, is often used to describe the T_2 of the sediment [*Peyron et al.*, 1996]. The use of T_{2LM} in place of T_2 assumes that the pore system can be represented as an equivalent porous medium in which the pores all have the same transverse relaxation time equal to T_{2LM}.

[8] Due to the relationship between T_2 and pore geometry, the SDR equation relates permeability to pore size and shape. We utilize this relationship to evaluate how A varies with lithology by comparing the SDR equation and Kozeny permeability model, which both assume a common fundamental relationship between permeability and pore surface area. Combining equations (1) and (3), the SDR equation can be re-expressed as

$$k = A\varphi^4 \frac{1}{\rho_2^2} \left(\frac{V}{S}\right)^2. \tag{4}$$

The Kozeny permeability model relates permeability to pore system structure by assuming that flow occurs through capillary tubes [*Bear*, 1972; *Scheidegger*, 1974]. The Kozeny equation [*Kozeny*, 1927; *Carman*, 1937] expresses permeability as

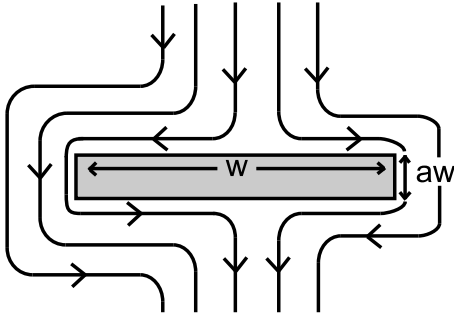$$k = \frac{\varphi}{\nu\tau^2} \left(\frac{V}{S}\right)^2, \tag{5}$$

Figure 2. Example clay grain. This grain has width w and aspect ratio a such that the grain's thickness is aw. Flow paths that encounter the particle from above, as illustrated, are deflected around the particle.

where τ is the tortuosity of the pore system [m m^{-1}] and ν is a dimensionless pore shape factor [m^2 m^{-2}]. Equating equations (4) and (5) and solving for A yields

$$A = \frac{\rho_2^2}{\varphi^3 \nu \tau^2}. \tag{6}$$

This expression for A incorporates properties of the pore system (φ, ν, τ) and intrinsic properties of the mineral grains (ρ_2). A rigorous computation of A requires knowledge of all these parameters.

2.2. Determining a Function for A

[9] The parameters ρ_2, ν, and τ in equation (6) are difficult to constrain, which presents an impediment to quantifying the lithologic variation of A. To overcome this obstacle, we relate these parameters to other sediment properties that are more easily measured and develop an equivalent expression to equation (6) that allows for easier computation of A.

[10] Transverse surface relaxivity ρ_2 is related to the presence of paramagnetic or ferromagnetic ions on the pore walls [*Kleinberg*, 1996; *Kleinberg et al.*, 2003]. Mn^{2+}, Fe^{2+}, and Fe^{3+} have the greatest effect on surface relaxivity, with larger amounts of these ions adsorbed to mineral surfaces correlated with higher surface relaxivities [*Kenyon and Kolleeny*, 1995]. Clay minerals such as chlorite and glauconite often contain iron and other paramagnetic/ferromagnetic ions [*Serra*, 1990; *Matteson et al.*, 2000], and clay-rich sediments have higher ρ_2 values than sediments with little or no clay [*Huang*, 1997]. ρ_2 is difficult to measure, and is often estimated by comparing T_2 distributions with pore throat distributions obtained from capillary pressure data [e.g., *Kleinberg*, 1996], which often requires some assumption of unrealistic pore geometries [e.g., *Zhang*, 2001]. Magnetic susceptibility relates the magnetization vector produced when a material is placed in an external magnetic field to the strength of the external field [*Santamarina et al.*, 2001]. Since the presence of paramagnetic and ferromagnetic ions will increase the magnetization vector, magnetic susceptibility increases with increasing paramagnetic/ferromagnetic ion concentration [*Dahlin and Rule*, 1993]. *Matteson et al.* [2000] further show that ρ_2 and magnetic susceptibility are positively correlated. Since magnetic susceptibility is an easily measurable quantity that is a function of the same properties as

ρ_2, we assume that ρ_2 can be represented by a linear function of magnetic susceptibility χ such that $\rho_2 = \alpha\chi + \beta$ where α and β are constants with units m s^{-1}. We assume a linear relationship between ρ_2 and χ for sake of simplicity in the absence of any constrained relationship between these terms.

[11] Tortuosity can be computed from a representative model of grain geometry. Clay mineral grains are typically plate-shaped, with aspect ratios (ratio of thickness to width) ranging from 0.1 to 0.003 [*Santamarina et al.*, 2002]. A fluid flow path that intersects a clay grain will be deflected around it, causing the flow path to be lengthened. If a grain has width w and aspect ratio a [m m^{-1}] (Figure 2), the maximum fluid flow path around the particle is $w(a + 1)$. Since the shortest distance across the particle is aw, the maximum tortuosity of a flow path deflected by the clay grain is

$$\tau = \frac{w(a+1)}{aw} = 1 + \frac{1}{a}. \tag{7}$$

[12] Specific surface S_a is the ratio of surface area to mass of solid material. If a clay grain extends unit length in the third dimension, the specific surface is

$$S_a = \frac{2aw + 2w + 2aw^2}{aw^2\rho_g} = \frac{2 + 2a(1 + w)}{aw\rho_g}. \tag{8}$$

where ρ_g is the grain density. Solving equation (8) for a and substituting into equation (7) yields

$$\tau = w\left(\frac{S_a\rho_g}{2} - 1\right). \tag{9}$$

To compute tortuosity, we assume that the average grain width w of a sample can be approximated by the median grain diameter D_{50} measured by standard granulometry techniques, and that the bulk specific surface of all the sediment grains is representative of individual grains. The use of D_{50} and S_a together allows for quantification of grain size and aspect ratio. The tortuosity of any flow path through the sediment τ_{bulk} is the spatially weighted average of flow paths that intersect sediment grains (equation (9)) and flow paths in free pore space, since the probability of a particle of fluid encountering free pore space is φ while the probability of its encountering a solid grain is $1 - \varphi$ [*Boudreau and Meysman*, 2006]. Free pore space has $\tau = 1$ because fluid flowing in free pore space is unimpeded and will take the shortest distance between points. This spatial averaging yields

$$\tau_{bulk} = \varphi + (1 - \varphi)D_{50}\left(\frac{S_a\rho_g}{2} - 1\right). \tag{10}$$

It should be noted that, by only considering flow perpendicular to the long axis of the grain, we are computing a maximum value of tortuosity for the system. In reality, sediment grains may be oriented in any direction with respect to the direction of flow. However, to the extent that a particle of fluid encountering sediment grains along its flow path is analogous with electrical current traveling through resistors in series, we assume that the maximum tortuosity controls the permeability of the system, and so the tortuosity
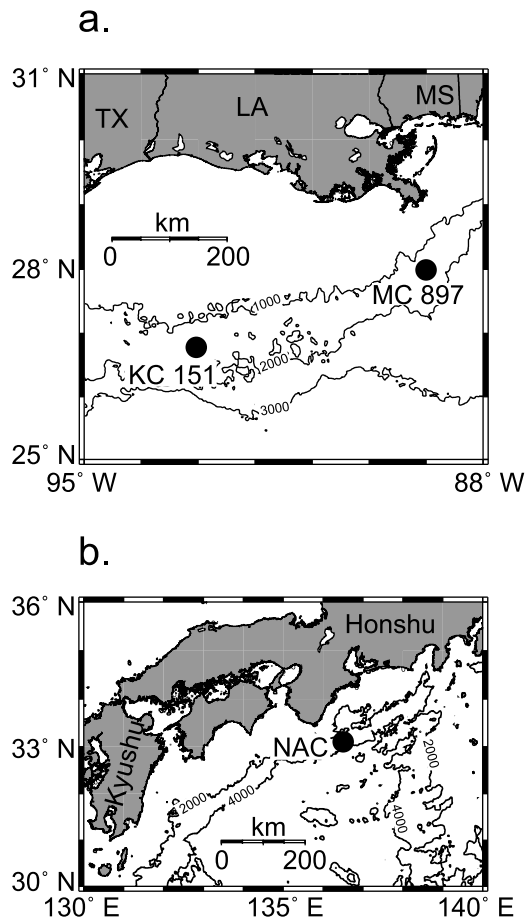
Figure 3. (a) Map showing location of Keathley Canyon Block 151 (KC 151) and Mississippi Canyon Block 897 (MC 897) in the northern Gulf of Mexico. (b) Map showing location of Nankai accretionary complex (NAC) offshore southern Honshu, Japan. Bathymetric contour interval is 1000 m on both maps.

from equation (10) is an appropriate approximation for use in equation (6).

[13] The remaining unknown in equation (6) is the pore shape factor ν, which describes the deviation of the cross-sectional shape of the pores from circular [*Bear*, 1972]. *Carman* [1937] reports values of ν for different pore cross-sectional shapes ranging from 1.67 for equilateral triangles to 3.0 for infinite rectangular slits; circular or elliptical pores have $\nu = 2.0$–2.5. *Happel and Brenner* [1983] similarly report little variation in ν for several computed grain geometries. Since the exact grain and pore geometries in mudstones are usually unknown, it is difficult to assign a value to ν. *Carman*'s [1937] assertion that a value of 2.5 is acceptable is based on calculations and experiments performed on packings of spherical particles. It is likely, however, that the grain and pore geometries of mudstones deviate significantly from these idealized cases. However, given the small variation in ν reported by *Carman* [1937] and the fact that ν has an exponent of 1 in equation (6) while ρ_2 and τ are both squared, we assume that changes in ν do not exert a significant influence on A compared with other properties like magnetic susceptibility and specific

surface. Therefore we opt to treat ν as a constant that is included in the constants α and β in the ρ_2-magnetic susceptibility relation. It is not important to know the exact value of ν since we are implicitly assuming that $\rho_2 = \alpha\chi + \beta = \nu^{1/2}(\alpha'\chi + \beta')$ where α' and β' are unconstrained fundamental values in the χ - ρ_2 relationship.

[14] Based on this analysis, we recast our expression for A (equation (6)) as

$$A = \frac{(\alpha\chi + \beta)^2}{\left(\varphi + (1 - \varphi)D_{50}\left(\frac{S_a\rho_g}{2} - 1\right)\right)^2 \varphi^3}, \quad (11)$$

where χ is magnetic susceptibility [$m^3 \, m^{-3}$], D_{50} is median grain diameter [m], S_a is specific surface [$m^2 \, kg^{-1}$], ρ_g is the solid grain density [$kg \, m^{-3}$], and α and β are constants that relate surface relaxivity and magnetic susceptibility. Equation (11) provides a relationship based on properties that may be easily and inexpensively measured in the laboratory as opposed to equation (6) which has the difficult-to-constrain parameters ρ_2, τ, and ν. The terms α and β require some calibration with sample data, but we expect that samples of similar lithology will be characterized by a unique (α, β) pair. We test equation (11) by comparing laboratory measurements of permeability, T_2 distribution, porosity, grain size, specific surface, and magnetic susceptibility for three suites of natural mudstones as well as resedimented mixtures of silica, bentonite, and kaolinite powders. We show that combining equations (1) and (11) extends the capability of permeability calculation from NMR logs to fine-grained, clay-rich sediments.

3. Samples

[15] We utilized natural mudstones from three different locations: Mississippi Canyon Block 897 (MC 897) and Keathley Canyon Block 151 (KC 151) in the northern Gulf of Mexico, and the Nankai accretionary complex offshore southeastern Japan (Figure 3). The samples from MC 897 were collected in Integrated Ocean Drilling Program (IODP) Expedition 308 hole U1324B and represent distal levee and hemipelagic drape deposits composed primarily of terrigenous clay and mud [*Flemings et al.*, 2006]. We selected three well-characterized intervals in the borehole in which grain-size measurements [*Sawyer et al.*, 2009] and mineral assemblages from X-ray diffraction [*John and Adatte*, 2009] were available, and used adjacent core material for resedimentation and dead-weight consolidation; each sample was dead-weight consolidated to two different stress levels to obtain measurements at different porosities.

[16] The samples from KC 151 were collected in the Department of Energy/Chevron Joint Industry Project hole KC151–3. The samples represent deposits from the flank of a salt withdrawal minibasin, and are interpreted as hemipelagic drape sediments with some higher-energy deposits (sands and mass wasting) related to subsidence of the basin and deposition during lowstand conditions [*Hutchinson et al.*, 2008]. Sediments are generally terrigenous clay and silty clay [*Winters et al.*, 2008]. We selected six samples for which permeability data exist [*Dugan*, 2008; *Daigle and Dugan*, 2009].

[17] The samples from the Nankai accretionary complex were collected in IODP Expedition 316 holes C0004C, C0006E, C0007C and C0008A. These samples represent slope and accretionary prism sediments; the lithology is complex and includes clay layers, volcanic ash, graded sand beds, and gravels [Screaton et al., 2009]. We selected four intact core samples for analysis, and resedimented and dead-weight consolidated two additional samples.

[18] In addition to natural samples, we used three industrial powders for resedimentation and dead-weight consolidation: Min-U-Sil® 40 silica powder and Snow*Tex® 45 calcined kaolin powder, both from U.S. Silica Company, and Volclay® 325 mesh sodium bentonite powder from American Colloid Company. We resedimented six mixtures of these materials, each of two components in different proportions, to produce samples with controlled mineralogy. Each mixture was dead-weight consolidated to two different stress levels to obtain measurements at different porosities.

4. Experimental Procedure

4.1. Resedimentation and Dead-Weight Consolidation

[19] Resedimented samples were prepared following the method of Mazzei [2008]. Samples were oven-dried at 60°C for 72 h and powdered with a ceramic mortar and pestle. The desired mass of powdered sediment was mixed with deionized water using an electric stand mixer until the mixture reached a thick but runny consistency. The mixture was then poured into a greased sedimentation cylinder and agitated to remove any air pockets. Porous stones were placed at the top and bottom of the sample to allow water drainage from both ends of the sample. Load was applied by a plunger inserted into a cross beam on which weights were placed. Vertical displacement of the load was monitored with linear variable displacement transducers (LVDTs). We considered each load increment to be complete when the LVDT measurements indicated the end of primary consolidation. We used load increments of 1 such that the load on the sample was doubled at each increment to reach the desired consolidation stress. We assume minimal flocculation in the natural sediments since the sediment is mixed as a slurry rather than settling out of a water column. A lack of flocculation in our sediments may cause them to have lower porosities and permeabilities than natural marine sediments consolidated to similar effective stress levels [Bennett et al., 1989; Velde, 1996], but should maintain permeability behavior similar to sediments that have been consolidated to the point where flocculates are no longer a dominant part of the pore networks.

4.2. T₂ Measurements

[20] We measured T_2 distributions for each sample using a Resonance Instruments MARAN-II device with a proton resonance frequency of 2.1 MHz. Measurements were performed on fully saturated, 3.8 cm diameter samples at 30°C. We used a Carr-Purcell-Meiboom-Gill (CPMG) pulse sequence with an echo spacing of 0.2 ms and a length of 1024 ms. We recorded 36 scans with 3 s dead time between scans. The T_2 distribution was computed from raw echoes using the stretched multiexponential approach [Peyron et al., 1996]. The T_{2LM} value reported for each sample is the geometric mean of this distribution.

[21] T_2 data for the samples from KC 151 were obtained in the field using Schlumberger's ProVISION™ logging-while-drilling (LWD) tool. Measurements were performed using two different echo spacings of 1.2 and 0.8 ms and a proton resonance frequency of 2.1 MHz. The depth of investigation of the tool is 7 cm in a 21.5 cm borehole, and the vertical resolution is 1–1.2 m [Alvarado et al., 2003]. The ProVISION™ data were correlated with the laboratory samples. Further details regarding NMR data from KC 151 are given by Daigle and Dugan [2009]. The differences in echo spacings, magnet size, and magnetic field gradient between the ProVISION™ and Maran do not affect the T_2 measurements since these parameters only affect relaxation by molecular diffusion, which in water-saturated sediments is much slower than relaxation due to interactions with paramagnetic ions [Kleinberg, 1999].

4.3. Permeability Measurements

[22] We measured permeability using constant rate-of-strain (CRS) consolidation experiments and flow-through tests in a flexible-wall permeameter. CRS consolidation experiments [ASTM International, 2006] were performed at room temperature (20°C). Samples were trimmed into a fixed-ring consolidation cell and placed in the consolidation chamber. The chamber was filled with distilled water and held under a constant back pressure of 0.39 MPa. We then consolidated the samples at a constant strain rate of 0.3 or 0.5%/hr to a maximum of 20% strain or 4.1 MPa total vertical stress, which is the limit of the load cell. The pore pressure at the base of the specimen was monitored passively and recorded during consolidation along with the total vertical stress required to maintain a constant strain rate.

[23] Permeability was computed from the excess pressure at the base of the sample during consolidation [ASTM International, 2006]:

$$k = \frac{\dot{\varepsilon} H H_0 \mu_w}{2 \Delta u}, \qquad (12)$$

where $\dot{\varepsilon}$ is strain rate [s^{-1}], H and H_0 are the instantaneous and initial heights of the sample [m], μ_w is the dynamic viscosity of water [Pa s], and Δu is the excess pressure at the base of the sample [Pa]. To determine the initial permeability value, we fit a log linear relationship between porosity and permeability [e.g., Neuzil, 1994] during virgin consolidation and extrapolated back to the initial porosity value (Figure 4). Initial porosity was determined by taking the difference between the initial mass of the sample and the mass of the sample after oven-drying assuming 100% initial water saturation [Blum, 1997]. We assumed that the difference in mass between the wet and dried sample was equal to the mass of water initially in the sample. We computed porosity by dividing the equivalent volume of water initially in the sample by the sum of the volumes of dried material and water. Dried material volume was computed from the final dry mass and solid grain density and assumed to be equal to the volume of solid grains. Errors reported for CRS consolidation experiments are standard errors for the φ-log$k$ fit.

[24] Flow-through permeability measurements were performed in a flexible-wall permeameter at room temperature (20°C) [ASTM International, 2004]. Samples (3.8 cm diameter, 4–5 cm height) were trimmed from the dead-
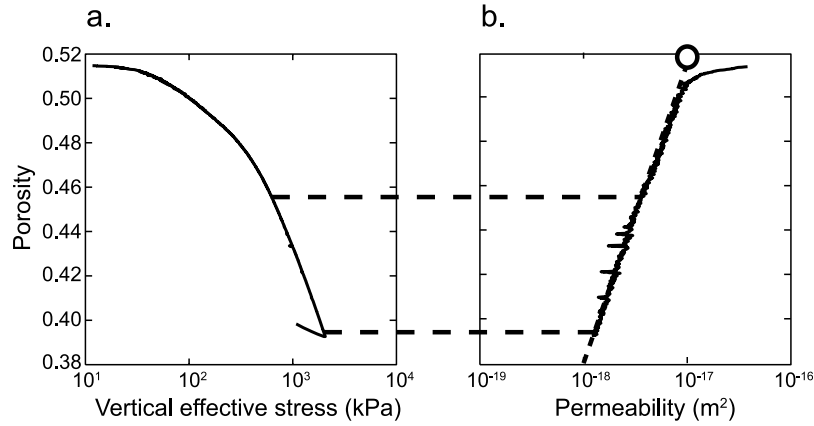
Figure 4. Example CRS experiment data for IODP Expedition 308 sample 26H-3 with regression to determine permeability. (a) Porosity-vertical effective stress data from the experiment. (b) Porosity-permeability data from the experiment computed from pressure data using equation (12). The virgin consolidation portion of the porosity-vertical effective stress curve is isolated (dashed lines), and a log linear regression is performed on the corresponding porosity-permeability data (dashed line in Figure 4b). The permeability errors reported in Table 1 are the standard deviation of this regression in porosity-log permeability space. This regression is then extrapolated to the initial porosity, which is determined by taking the saturated and dry masses of the sample. In this case the initial porosity was 0.520, and the corresponding permeability was 9.80×10^{-18} m^2.

weight consolidated sediment. We placed the samples in the permeameter chamber with porous stones at the top and base and sealed the samples in latex membranes. Flow lines were connected to the top and base of the sample. The permeameter chamber was filled with distilled water, and we applied a chamber pressure of 34 kPa to ensure complete contact of the membrane on the sample. We then increased the pressure in the sample and in the chamber by 340 kPa while maintaining the 34 kPa effective stress, and let the sample equilibrate for at least 8 h to ensure complete saturation. After pressuring the sample, we flowed deaired water through the sample by applying a pressure difference of 21 kPa across the sample. Permeability was computed from Darcy's law:

$$k = \frac{Q\mu_w H}{B\Delta P}, \tag{13}$$

where Q is the volumetric flow rate [m^3 s^{-1}], H is the height of the sample [m], B is the cross-sectional area of the sample [m^2], and ΔP is the pressure difference across the sample [Pa]. Experiments were run for at least 24 h to ensure that the system achieved steady state; reported permeability values are the mean of the steady state portion of the permeability data (Figure 5). Errors reported for flow-through permeameter measurements are the standard deviation of the steady state portion of the data. Comparison of flow-through permeability data and CRS permeability data for the Nankai accretionary complex sediments [*Dugan and Daigle*, 2011] shows that the methods yield statistically indistinguishable permeability values.

4.4. Specific Surface Measurement

[25] We measured specific surface using the spot-test method of methylene blue adsorption [*Santamarina et al.*, 2002]. One gram of methylene blue powder ($C_{16}H_{18}ClN_3S$)

is mixed with 200 mL distilled water and added in 0.5 mL increments to a mixture initially consisting of 10 g of oven-dried (60°C for 72 h), powdered sediment and 30 mL of distilled water. Precise increment volumes are obtained by using a graduate pipette. The mixture is stirred thoroughly with a magnetic stirrer after each methylene blue increment. After stirring, a drop of the mixture is placed on Fisherbrand filter paper P5. When all the mineral surfaces in the mixture have been coated with methylene blue, excess methylene blue in the mixture will bleed away from the drop placed on the
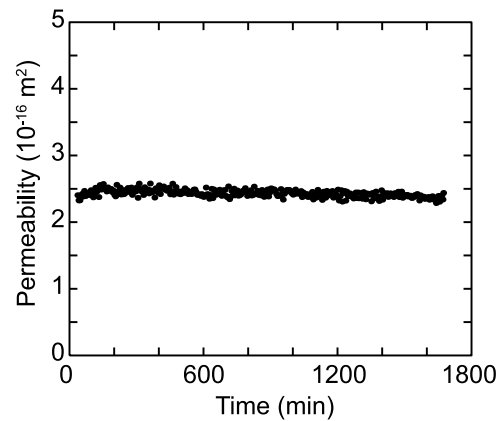
Figure 5. Example permeameter experiment data for IODP Expedition 316 sample 3H-2. Permeability is determined at 5 min intervals during the experiment from equation (13) using pump pressure and flow rate data. The permeability value for the sample is the average of the steady state portion of the data, which in this case was all but the first 60 min of the experiment. The reported error for the permeability is the standard deviation of the data used to determine permeability.

filter paper. The number of increments to reach this endpoint is then used to compute the specific surface:

$$S_a = \frac{1}{M_m}\frac{1}{200}0.5NA_vA_{MB}\frac{1}{10}, \tag{14}$$

where M_m is the molar mass of methylene blue (319.87 g mol^{-1}), N is the number of methylene blue increments, A_v is Avogadro's number (6.022×10^{23} mol^{-1}), and A_{MB} is the mineral surface area covered by one molecule of methylene blue (1.3×10^{-18} m^2). Errors for specific surface measurements are equal to the difference in S_a between 0.5 mL increments (0.6 m^2 g^{-1}).

[26] For the samples composed of industrial powders, we measured S_a for the individual powders and then computed S_a for the resulting mixture based on mass fraction of each component in the mixture. We obtained $S_a = 1800 \pm 300$ m^2 kg^{-1} for Min-U-Sil, $S_a = 9200 \pm 300$ m^2 kg^{-1} for Snow*Tex, and $S_a = 3.85 \pm 0.3 \times 10^5$ m^2 kg^{-1} for Volclay. These values are consistent with typical values for kaolinite and smectite reported by *Santamarina et al.* [2002].

4.5. Grain Size

[27] Grain size distributions were determined for the Nankai accretionary complex and silica-kaolinite powder samples using Stokes settling analysis [*ASTM International*, 2003]. Samples were dried for 72 h at 60°C. Each sample (20–40 g) was then mixed with 125 mL deionized water and 5 g sodium hexametaphosphate deflocculant, and allowed to sit at least 16 h. The mixture was then mixed for 1 min using a Hamilton Beach milkshake mixer to disperse the sample, and poured into a sedimentation cylinder and covered with enough deionized water to make 1 L of solution. The solution was then agitated in the sedimentation cylinder for 1 min and left to settle. During settling of the particles, the density of the solution was measured periodically using ASTM hydrometer 151H. The grain size distribution by mass was calculated from the change in density of the mixture over time from Stokes' law of settling. The median grain size D_{50} is the median of the grain size distribution by mass. Grain size distributions for the samples from MC 897 were measured by *Sawyer et al.* [2009] using Stokes settling analysis. D_{50} was determined for the samples from KC 151 by *Winters et al.* [2008] using Coulter Counter data. The grain size distribution for Volclay was measured by laser diffraction using a Malvern Mastersizer 2000.

4.6. Magnetic Susceptibility

[28] Volume magnetic susceptibility measurements were performed shipboard on whole-round cores for the samples from MC 897, KC151, and the Nankai accretionary complex using an 80 mm diameter Bartington loop sensor [*Expedition 308 Scientists*, 2006; *Schultheiss et al.*, 2006; *Expedition 316 Scientists*, 2009]. Values for these samples were corrected for porosity by dividing by $(1 - \varphi)$ using the porosity recorded by the shipboard core logger; we neglected the effects of the pore water since the volume magnetic susceptibility of water is two orders of magnitude less than the lowest values in our sample set [*Hürlimann*, 1998]. Magnetic susceptibilities for the laboratory mixtures were computed using the formula

$$\chi = \rho_g(x_1\chi_{m1} + x_2\chi_{m2}), \tag{15}$$

where x_1 and x_2 are the mass fractions of the two mineral constituents and χ_{m1} and χ_{m2} are the mass magnetic susceptibilities of the two mineral constituents [m^3 kg^{-1}], and ρ_g is the grain density of the mixture [kg m^{-3}]. For Snow*Tex we assumed $\chi_m = 3.1 \times 10^{-6}$ m^3 kg^{-1}, the literature value for pure kaolinite [*Schreiner et al.*, 2002]. For Volclay we assumed $\chi_m = 3.1 \times 10^{-6}$ m^3 kg^{-1}, the literature value for Wyoming bentonite [*Bachir*, 2009]. For Min-U-Sil we assumed $\chi_m = -1.6 \times 10^{-5}$ m^3 kg^{-1}, the value for pure silica [*Lide*, 2009].

4.7. Determination of A

[29] For each sample, we computed A by inverting equation (1) and using the measured permeability, porosity, and T_{2LM} values. Porosities were determined by weighing samples when fully saturated at the end of deadweight consolidation, oven-drying at 60°C for at least 72 h, and comparing the mass of the dried sample with the mass of the wet sample. Errors reported for A are determined from the reported errors for permeability measurements by the formula $\Delta A = \Delta k/\varphi^4 T_{2LM}^2$ where ΔA is the error for A and Δk is the error for permeability. The porosity values for our laboratory samples have an error of ± 0.0005 m^3 m^{-3}, or <0.1% error relative to the porosity values themselves, and we ignore this contribution to the error in A since it is much smaller than the error in the permeability data, which is generally $\pm$3–50% (Table 1). In practice, however, porosity may be estimated from log data, which may have significant error due to borehole conditions or assumptions of matrix or fluid properties. A relative uncertainty in porosity data of 10% (0.50 versus 0.55 m^3 m^{-3}, for example) would result in a relative error of 45% in the computed value of A since porosity is raised to the 4th power. Care must therefore be taken when evaluating log-derived properties.

5. Results

[30] Measured porosity, T_{2LM}, permeability, specific surface, median grain size, and magnetic susceptibility for all samples are shown in Table 1. T_{2LM} values for all samples span nearly two orders of magnitude, ranging from 1.19 to 41.76 ms. The resedimented mixtures of silica and kaolinite have the largest T_{2LM} values, in the range of 20–40 ms, while the samples from MC 897 have the smallest T_{2LM} values (<2.5 ms). All other samples have T_{2LM} generally on the order of a few milliseconds.

[31] Permeability values range from 4.29×10^{-15} m^2 to 1.66×10^{-18} m^2, spanning nearly four orders of magnitude. The resedimented silica-kaolinite mixtures and the samples from the Nankai accretionary complex have the highest permeabilities, generally on the order of 10^{-15} to 10^{-16} m^2. The samples from KC 151, MC 897, and the resedimented silica-bentonite mixtures have permeabilities on the order of 10^{-17} to 10^{-18} m^2. The pattern of permeability values matches that of the T_{2LM} values, with higher permeability correlated with larger T_{2LM} values, except in the case of the Nankai accretionary complex samples, which have small T_{2LM} but high permeability.

[32] Specific surface values range from 3300 to 193400 m^2 kg^{-1}. Variation in specific surface is driven by variations in mineralogy. The resedimented silica-kaolinite mixtures have the smallest specific surface, between 3300

Table 1. Data for All Samples Used for This Study[a]

Composition	Sample Type	φ (m³ m⁻³)	T_{2LM} (s)	Measured k (m²)	Perm Error (m²)	Permeability Test Type	S_a (m² kg⁻¹)	ρ_g (kg m⁻³)	D_{50} (m)	χ (m³ m⁻³)	A (m² s⁻²)	Computed A (m² s⁻²)	Computed k (m²)	SDR k (m²)
80% Silica 20% Kaolinite	Resed.	0.318	0.034	4.31×10^{-16}	7.42×10^{-17}	CRS	3300	2634	8.40×10^{-6}	-3.46×10^{-2}	$3.65 \pm 0.63 \times 10^{-2}$	4.21×10^{-11}	4.98×10^{-16}	2.61×10^{-16}
80% Silica 20% Kaolinite	Resed.	0.335	0.0418	7.51×10^{-16}	8.18×10^{-16}	CRS	3300	2634	8.40×10^{-6}	-3.46×10^{-2}	$3.43 \pm 1.78 \times 10^{-2}$	3.78×10^{-11}	8.30×10^{-16}	4.84×10^{-16}
50% Silica 50% Kaolinite	Resed.	0.380	0.0251	4.09×10^{-16}	1.13×10^{-17}	Flow-through	5500	2609	4.58×10^{-6}	-2.14×10^{-2}	$3.11 \pm 0.09 \times 10^{-2}$	2.17×10^{-11}	2.86×10^{-16}	2.90×10^{-16}
50% Silica 50% Kaolinite	Resed.	0.388	0.0244	3.06×10^{-16}	6.53×10^{-17}	CRS	5500	2609	4.58×10^{-6}	-2.14×10^{-2}	$2.28 \pm 0.49 \times 10^{-2}$	2.09×10^{-11}	2.80×10^{-16}	2.95×10^{-16}
25% Silica 75% Kaolinite	Resed.	0.479	0.0213	5.10×10^{-16}	1.07×10^{-16}	CRS	7300	2590	2.36×10^{-6}	-1.06×10^{-2}	$2.14 \pm 0.04 \times 10^{-2}$	1.83×10^{-11}	4.37×10^{-16}	5.27×10^{-16}
25% Silica 75% Kaolinite	Resed.	0.496	0.0244	5.48×10^{-16}	1.66×10^{-16}	CRS	7300	2590	2.36×10^{-6}	-1.06×10^{-2}	$1.52 \pm 0.46 \times 10^{-2}$	1.75×10^{-11}	6.32×10^{-16}	7.97×10^{-16}
100% Kaolinite	Resed.	0.550	0.0259	4.31×10^{-16}	3.19×10^{-17}	CRS	9200	2570	1.68×10^{-6}	3.14×10^{-6}	$7.01 \pm 0.52 \times 10^{-2}$	9.22×10^{-12}	5.67×10^{-16}	1.36×10^{-15}
100% Kaolinite	Resed.	0.543	0.0246	4.31×10^{-16}	1.57×10^{-16}	CRS	9200	2570	1.68×10^{-6}	3.14×10^{-6}	$8.20 \pm 2.99 \times 10^{-2}$	9.31×10^{-12}	4.90×10^{-16}	1.16×10^{-15}
85% Silica 15% Bentonite	Resed.	0.581	0.0135	4.45×10^{-18}	1.88×10^{-19}	CRS	59300	2657	9.68×10^{-6}	-3.69×10^{-2}	$2.14 \pm 0.09 \times 10^{-3}$	2.72×10^{-13}	5.64×10^{-18}	5.03×10^{-18}
85% Silica 15% Bentonite	Resed.	0.513	0.0081	1.66×10^{-18}	2.11×10^{-19}	CRS	59300	2657	9.68×10^{-6}	-3.69×10^{-2}	$3.62 \pm 0.46 \times 10^{-3}$	2.92×10^{-13}	1.34×10^{-18}	1.11×10^{-18}
50% Silica 50% Bentonite	Resed.	0.791	0.0103	6.24×10^{-18}	2.79×10^{-19}	CRS	193400	2675	6.15×10^{-6}	-2.18×10^{-2}	$1.52 \pm 0.07 \times 10^{-3}$	2.22×10^{-13}	9.13×10^{-18}	9.99×10^{-18}
IODP308 U1324B 26H-3 127–142 cm	Resed.	0.493	0.0015	5.98×10^{-18}	2.53×10^{-19}	CRS	83200	2700	7.60×10^{-7} (5)	1.61×10^{-3}	$4.76 \pm 0.21 \times 10^{-1}$	6.90×10^{-11}	8.66×10^{-18}	4.56×10^{-18}
IODP308 U1324B 26H-3 127–142 cm	Resed.	0.520	0.0012	9.80×10^{-18}	7.01×10^{-19}	CRS	83200	2700	7.60×10^{-7} (5)	1.61×10^{-3}	$9.48 \pm 0.68 \times 10^{-1}$	6.54×10^{-11}	6.76×10^{-18}	3.76×10^{-18}
IODP308 U1324B 4H-7 65–78 cm	Resed.	0.565	0.0023	1.65×10^{-17}	4.23×10^{-19}	CRS	113200	2700	1.46×10^{-6} (5)	9.72×10^{-4}	$3.21 \pm 0.08 \times 10^{-1}$	3.06×10^{-11}	1.57×10^{-17}	1.87×10^{-17}
IODP308 U1324B 4H-7 65–78 cm	Resed.	0.518	0.0018	3.28×10^{-18}	2.59×10^{-19}	CRS	113200	2700	1.46×10^{-6} (5)	9.72×10^{-4}	$1.50 \pm 0.12 \times 10^{-1}$	3.25×10^{-11}	7.13×10^{-18}	7.97×10^{-18}
IODP308 U1324B 7H-7 14–29 cm	Resed.	0.568	0.0023	9.53×10^{-18}	3.12×10^{-19}	CRS	138300	2700	2.09×10^{-6} (5)	9.29×10^{-4}	$1.81 \pm 0.06 \times 10^{-1}$	1.07×10^{-11}	5.65×10^{-18}	1.91×10^{-17}
IODP308 U1324B 7H-7 14–29 cm	Resed.	0.530	0.0018	2.57×10^{-18}	1.71×10^{-19}	CRS	138300	2700	2.09×10^{-6} (5)	9.29×10^{-4}	$1.04 \pm 0.07 \times 10^{-1}$	1.11×10^{-11}	2.75×10^{-18}	8.99×10^{-18}
KC151 10C-3 70–74 cm	Natural	0.447	0.0033	1.50×10^{-17}	1.74×10^{-19}	CRS (1)	67900 (2)	2700	2.01×10^{-6} (6)	3.55×10^{1}	$3.56 \pm 0.10 \times 10^{-11}$	3.83×10^{-11}	1.61×10^{-17}	1.41×10^{-17}
KC151 ¹⁴C-1 55–59 cm	Natural	0.456	0.0033	3.41×10^{-17}	1.44×10^{-19}	CRS (1)	71000 (2)	2700	1.72×10^{-6} (6)	3.76×10^{1}	$7.48 \pm 0.09 \times 10^{-11}$	4.82×10^{-11}	2.20×10^{-17}	1.53×10^{-17}
KC151 15C-3 40–45 cm	Natural	0.424	0.0034	8.11×10^{-18}	1.70×10^{-19}	CRS (2)	100300 (3)	2700	1.86×10^{-6} (6)	2.83×10^{1}	$2.23 \pm 0.11 \times 10^{-11}$	1.95×10^{-11}	7.09×10^{-17}	1.22×10^{-17}
KC151 19H-5 68–73	Natural	0.511	0.0034	6.82×10^{-18}	1.11×10^{-19}	CRS (1)	116300 (2)	2700	1.45×10^{-6} (6)	3.73×10^{1}	$8.65 \pm 0.52 \times 10^{-12}$	2.21×10^{-11}	1.74×10^{-17}	2.64×10^{-17}
KC151 20H-5 69–73 cm	Natural	0.511	0.0034	3.07×10^{-17}	7.88×10^{-19}	CRS (1)	120500 (2)	2700	1.51×10^{-6} (6)	6.01×10^{1}	$3.84 \pm 0.05 \times 10^{-11}$	2.72×10^{-11}	2.17×10^{-17}	2.68×10^{-17}
KC151 22C-3 9.6–14.6 cm	Natural	0.470	0.0032	1.08×10^{-17}	2.52×10^{-19}	CRS (2)	119300 (2)	2700	1.80×10^{-6} (6)	7.46×10^{1}	$2.13 \pm 0.08 \times 10^{-11}$	2.60×10^{-11}	1.32×10^{-17}	1.70×10^{-17}
IODP316 C0004C 3H-2 10–15 cm	Natural	0.622	0.0087	2.43×10^{-16}	5.42×10^{-18}	Flow-through	28100	2670 (4)	3.41×10^{-6} (7)	3.35×10^{-4}	$2.15 \pm 0.05 \times 10^{-10}$	4.12×10^{-11}	4.65×10^{-16}	5.51×10^{-15}
IODP316 C0004C 7H-9 10–15 cm	Natural	0.617	0.0071	2.24×10^{-16}	3.05×10^{-17}	Flow-through	15900	2670 (4)	2.78×10^{-6} (7)	5.03×10^{-4}	$3.10 \pm 0.42 \times 10^{-10}$	2.42×10^{-10}	1.75×10^{-15}	3.53×10^{-15}
IODP316 C0007C 10X-1 123–127.5 cm	Natural	0.455	0.0022	4.16×10^{-16}	2.22×10^{-17}	Flow-through	15300	2700 (4)	4.24×10^{-6} (7)	4.82×10^{-3}	$2.09 \pm 0.11 \times 10^{-9}$	2.32×10^{-9}	4.62×10^{-16}	9.72×10^{-17}
IODP316 C0006E 1H-3 98–102 cm	Natural	0.535	0.011	4.29×10^{-15}	3.26×10^{-16}	Flow-through	21400	2700 (4)	2.56×10^{-5} (7)	2.15×10^{-2}	$4.29 \pm 0.33 \times 10^{-10}$	4.27×10^{-10}	4.27×10^{-15}	4.89×10^{-15}
IODP316 C0008A 4H-6 34–39 cm	Resed.	0.577	0.005	2.01×10^{-16}	1.39×10^{-17}	Flow-through	24500	2700 (4)	3.97×10^{-6} (7)	3.47×10^{-4}	$7.26 \pm 0.50 \times 10^{-11}$	4.01×10^{-11}	1.11×10^{-16}	1.35×10^{-15}
IODP316 C0004C 9H-2 53–59 cm	Resed.	0.546	0.0036	3.30×10^{-16}	1.15×10^{-17}	Flow-through	19600	2670 (4)	4.03×10^{-6} (7)	1.18×10^{-3}	$2.85 \pm 0.10 \times 10^{-10}$	1.76×10^{-11}	2.04×10^{-16}	5.64×10^{-16}

[a]Here φ, porosity; T_{2LM}, geometric mean of transverse relaxation times; k, permeability; S_a, specific surface; ρ_g, grain density; D_{50}, median grain size; χ, magnetic susceptibility; A, SDR equation premultiplier. Computed permeability values are reported using the method described in this paper (computed k) as well as the conventional SDR equation (SDR k). Sources are indicated by the number in parentheses: 1, Dugan [2008]; 2, Daigle and Dugan [2009]; 3, Yun et al. [2006]; 4, Screaton et al. [2009]; 5, Sawyer et al. [2009]; 6, Winters et al. [2008]; 7, Dugan and Daigle [2011].

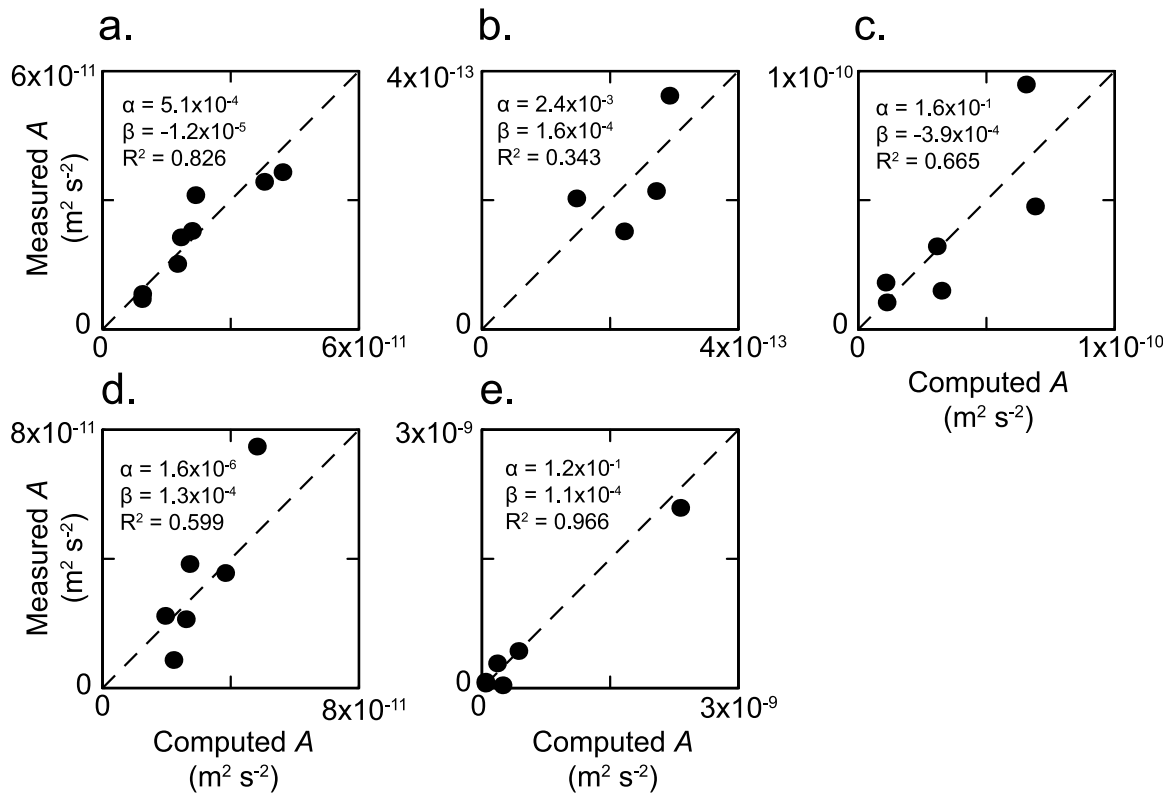**Figure 6.** Computed values of A from equation (11) plotted against values of A determined from measurements of permeability, T_{2LM}, and porosity. Input values for equation (11) are listed in Table 1. Values of α and β determined by error minimization for each sample set are listed on each plot along with R^2 values. The dashed line on each plot represents the line of 1:1 equivalence. (a) Silica-kaolinite samples. (b) Silica-bentonite samples. (c) Mississippi Canyon Block 897 samples. (d) Keathley Canyon Block 151 samples. (e) Nankai accretionary complex samples. Excluding the rightmost point in Figure 6e with measured $A = 2.09 \times 10^{-9}$ m^2 s^{-2} does not significantly alter the results and still yields a good fit with $R^2 = 0.904$. The poor fit in the silica-bentonite samples (Figure 6b) is attributed to interlayer water causing grain swelling in smectite and changing grain surface area exposed to flow in an unpredictable way.

and 9300 m^2 kg^{-1}, while the resedimented silica-bentonite mixtures have the largest specific surface, up to 193400 m^2 kg^{-1}. The samples from KC 151 and MC 897 have specific surface between 67900 and 138300 m^2 kg^{-1}, consistent with their dominantly hemipelagic sediment composition [*Flemings et al.*, 2006; *Hutchinson et al.*, 2008], while the samples from the Nankai accretionary complex have specific surface between 15300 and 28100 m^2 kg^{-1}, consistent with imma-ture, unweathered active volcanic margin sediments com-posed of larger grains [*Screaton et al.*, 2009]. The pattern of specific surface values matches the pattern of the perme-ability values, with low specific surface generally correlated with high permeability (e.g., silica-kaolinite mixtures) and high specific surface generally correlated with low perme-ability (e.g., KC 151, MC 897).

[33] Median grain size (D_{50}) values range from 0.76 to 9.68 μm. The samples from MC 897 and KC 151 generally have smaller median grain sizes than the other samples, indicating greater proportions of clay-sized grains in these samples.

[34] Magnetic susceptibility varies widely among the samples, ranging from −0.0369 to 74.6 m^3 m^{-3}. Values

within each of the five sample sets are generally of the same order of magnitude, but the variation among sample sets is quite large. This is probably due to variations in mineralogy, particularly in the abundance of iron-bearing minerals. Magnetic susceptibility values for the resedimented silica-kaolinite and silica-bentonite mixtures ranges between negative and positive values, which is due to the abundance of silica, a diamagnetic mineral [*Lide*, 2009]. The samples from KC 151 have the highest magnetic susceptibility values, suggesting that these samples have higher abundances of iron-bearing minerals than the other samples.

[35] We determined the constants α and β (equation (11)) for each sample set (silica-kaolinite, silica-bentonite, MC

Table 2. The α and β Parameters for Equation (11) Along With R^2 Coefficients for the Five Sample Sets Used in This Study

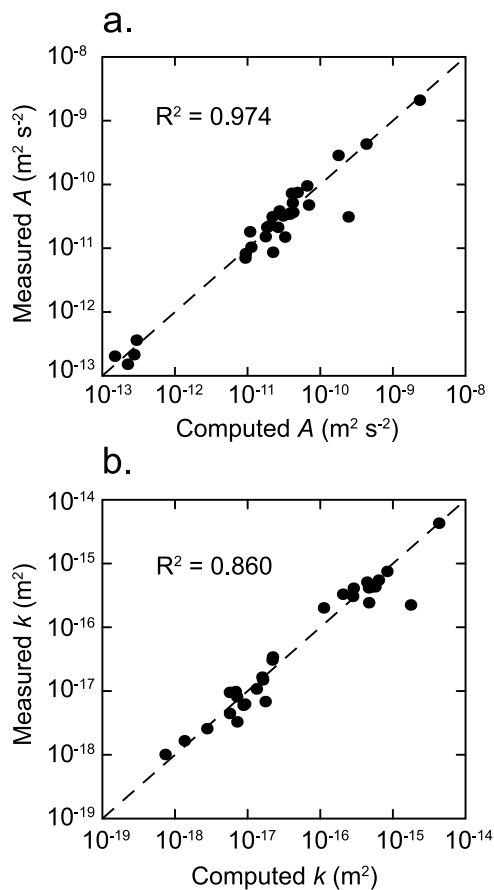| Sample Set	α (m s^{-1})	β (m s^{-1})	R^2
Silica-Kaolinite	5.1×10^{-4}	-1.2×10^{-5}	0.826
Silica-Bentonite	2.4×10^{-3}	1.6×10^{-4}	0.343
MC 897	1.6×10^{-1}	-3.9×10^{-4}	0.665
KC 151	1.6×10^{-6}	1.3×10^{-4}	0.599
Nankai	1.2×10^{-1}	1.1×10^{-4}	0.966

Figure 7. (a) Computed values of *A* from equation (11) plotted against measured values of *A* for all samples. Dashed line represents 1:1 equivalence. Equation (11) reproduces the measured values of *A* to a high degree of accuracy ($R^2 = 0.974$) with the appropriate values of α and β. (b) Computed permeability plotted against measured permeability for all samples. Permeability computations were made using equation (1) with measured porosity, T_{2LM}, and *A* computed from equation (11). The computed permeability matches the measured permeability to a high degree of accuracy ($R^2 = 0.860$) over nearly four orders of magnitude of permeability.

897, KC 151, Nankai accretionary complex) by error minimization of equation (11) (Figure 6). Because the term in the numerator of equation (11) is squared, this produces two unique sets of values, (α, β) and $(-\alpha, -\beta)$. We choose the set of values in which $\alpha > 0$ since this matches the relationship between χ and ρ_2 inferred from *Matteson et al.* [2000]. α and β values for each sample set along with R^2 coefficients of determination are summarized in Table 2.

[36] The measured and computed values of *A* for each sample set are generally in good agreement ($R^2 = 0.599-0.966$) except for the silica-bentonite mixtures ($R^2 = 0.343$; Figure 6b). We attribute this to the significant quantity of interlayer water present in smectite [*Santamarina et al.*, 2002], which changes the grain surface area exposed to fluid flow in an unpredictable way. Grain and pore geometry in the silica-bentonite samples could additionally be altered by the use of deionized water in resedimentation, since

bentonite particles have the tendency to swell when saturated with fresh water [e.g., *Slade et al.*, 1991; *Baker et al.*, 1993]. Using the appropriate α and β for each sample set in equation (11) matches the observed *A* value with $R^2 = 0.974$ (Figure 7a), and using the computed *A* values from equation (11) to calculate permeability from equation (1) matches the observed permeability with $R^2 = 0.860$ (Figure 7b). Included in Table 1 are permeability values obtained using the conventional SDR equation (equation (1)) by determining the single value of *A* that best fits the T_{2LM}, φ, and *k* data for each sample set. The permeability values computed with this technique have a poorer fit to the measured permeability, with $R^2 = 0.00636$. Thus we conclude that our model yields significantly more accurate permeability values than the conventional SDR technique in fine-grained sediments.

6. Discussion

6.1. Magnetic Susceptibility and Surface Relaxivity

[37] The variation in α and β among sample sets is due both to differences in mineralogy and differences in grain size and shape, but for samples of similar mineralogy, a single (α, β) pair describes the behavior of χ, ρ_2, and ν. The parameters α and β are independent of porosity and pore geometry since ν is assumed constant and χ and ρ_2 are properties of the solid mineral grains. Samples of similar mineralogy should exhibit the same $\chi - \rho_2$ behavior, since both quantities respond to changes in paramagnetic/ferromagnetic ion concentrations on mineral grains. Samples of similar grain shape and geometry should have similar ν values because changes in grain size, porosity, or relative abundance of different grains should cause the pore system to change self-similarly, as demonstrated by models of flow through packed beds of random particles [e.g., *Martys et al.*, 1994; *Coelho et al.*, 1997]. Constraining α and β requires only a small number of measurements. Among the five sample sets used in this study, α and β vary by several orders of magnitude (Table 2), which reflects the variability of magnetic susceptibility among the samples, and highlights the necessity of determining α and β regularly for permeability sample sets.

6.2. Model Validation

[38] Our model represents an improvement to the SDR equation (equation (1)) to allow for accurate permeability prediction in a variety of different sediments types. However, it is important to test whether the improved model yields comparable results for rocks in which the original SDR equation works well. The standard value of $A = 4 \times 10^{-9}$ m^2 s^{-2} [*Kenyon et al.*, 1995] is based on measurements performed on clean, reservoir-quality sandstones [*Kenyon et al.*, 1988], and is an appropriate value for Berea sandstone [*Kleinberg et al.*, 2003]. Berea sandstone typically has $\varphi = 0.18$, $D_{50} = 1.2 \times 10^{-4}$ m [*Caruso et al.*, 1985], $\rho_g = 2631$ kg m^{-3} [*Hiltl et al.*, 1999], $\chi = -4.0 \times 10^{-5}$ [*Hürlimann*, 1998] and $S_a = 100$ m^2 kg^{-1}. The typical mineral constituents of Berea are mainly quartz and kaolinite with minor accessory minerals [e.g., *Caruso et al.*, 1985; *Bernabe and Brace*, 1990; *Sayers et al.*, 1990; *Menéndez et al.*, 1996], so we apply the silica-kaolinite model to compute *A*. Using the properties listed above in equation (11), we obtain $A = 4.9 \times 10^{-9}$ m^2 s^{-2},

which is within 22.5% of the accepted value. This value of A yields $k = 4.0 \times 10^{-14}$ m^2 using the measured T2LM and porosity for the sample shown in Figure 1 ($\varphi = 0.18$, $T_{2LM} = 0.084$ s). This value is reasonably close to the measured value $k = 5.7 \times 10^{-14}$ m^2 obtained by flow-through measurement. Our model thus is able to replicate the expected value for clean sandstone, and additionally allows us to compute A for a range of other lithologies.

6.3. Differences Between the Kozeny and SDR Equations

[39] In our development of the expression for A (equation (11)), we assume that the Kozeny and SDR equations are equivalent. However, a key difference between the SDR equation (equation (1)) and the Kozeny equation (equation (5)) exists in the exponent on the porosity term. The SDR equation is a function of porosity to the 4th power while the Kozeny equation is a linear function of porosity. The linear dependence of porosity in the Kozeny equation arises due to its derivation from the Navier-Stokes equations for flow of a Newtonian fluid in capillary tubes, since the fluid velocity in the pores must be multiplied by porosity to obtain the macroscopic velocity of fluid through the porous medium for use in Darcy's law [*Scheidegger*, 1974]. Some of the earliest work on permeability from NMR data [e.g., *Seevers*, 1966] did correlate permeability with porosity to the 1st power; however, in the SDR equation (equation (1)) porosity is raised to the 4th power because it improves the statistical fit between NMR data and permeability measurements [*Banavar and Schwartz*, 1987; *Kenyon et al.*, 1988; *Straley et al.*, 1994]. There is some physical reasoning for raising porosity to the 4th power that accounts for the difference between the SDR and Kozeny equations.

[40] In water-saturated porous media, T_2 can be approximated as $(1/\rho_2)(V/S)$. To equate the SDR and Kozeny equations, the volume V and surface area S in the Kozeny and SDR equations must be the same and equal to the pore volume and pore surface area, respectively. However, by using the geometric mean of the T_2 distribution T_{2LM}, the SDR equation treats the porous medium as if it were composed of pores of a single size whose T_2 values are equal to T_{2LM}. Thus the SDR equation computes permeability in terms of some geometrically averaged V/S while the Kozeny equation computes permeability in terms of V/S for the pore system as a whole. In porous media in which the pores are all the same size, the V/S ratios will be equivalent. However, in porous media with a distribution of different pore sizes, this may not be the case. This discrepancy can be corrected by dimensional analysis of the two equations [e.g., *Kenyon et al.*, 1988; *Watson and Chang*, 1997]. Since permeability has dimensions of length squared, k in a porous medium can be viewed as proportional to the square of a representative length scale of the porous medium which can be represented by V/S since this quantity has units of length, so $k \propto (V/S)^2$. If the length scales in the Kozeny and SDR equations are represented by V/S_k and V/S_{NMR}, then NMR permeability k_{NMR} and Kozeny permeability k_k are related by

$$k_k \propto \left(\frac{V/S_k}{V/S_{NMR}} \right)^2 k_{NMR}. \qquad (16)$$

As a rock is consolidated, porosity and pore size will decrease. This decrease in pore size results in a corresponding decrease in V/S. As porosity decreases, V/S_k decreases more rapidly than V/S_{NMR} because the V term in the Kozeny equation represents the entire pore volume while in the SDR equation it only represents a small population of pores. We can thus postulate that the ratio of V/S_k and V/S_{NMR} is proportional to φ^m where m is some unknown exponent. *Dashen et al.* [1987] and *Kenyon et al.* [1988] show that the exponent m is equal to 2, and this accounts for the exponent of 4 that appears on porosity in the SDR equation. This term thus acts to translate the NMR length scale to a permeability length scale, and allows us to equate the SDR and Kozeny equations to find an expression for A in terms of NMR and pore system properties (equation (11)).

6.4. Strengths and Implications of Improved Permeability Model

[41] Our permeability model allows for improved accuracy in permeability calculations over roughly 4 orders of magnitude in fine-grained, clay-rich mudstones. The model requires only a few data points for calibration of the parameters α and β, and utilizes data which are easily measured. We have tested the model over a wide range of lithology and grain sizes, and the computed permeabilities match the measured values well ($R^2 = 0.860$). While the model does not return perfect results, it represents a significant improvement in computing permeability from NMR data in mudstones. In developing our algorithm for computing the parameter A, we showed that the Kozeny permeability model may be an appropriate description of mudstones. Specifically, we showed that the surface area and magnetic susceptibility are important properties that affect the NMR tool response in sediments with significant clay mineral content. The model further matches the measured permeability in Berea sandstone, showing that it is compatible with conventional NMR permeability techniques and works in clean, low-surface-area lithologies.

[42] The permeabilities and porosities of the samples used in this study are in the high end of the range of clay and mudstone permeability and porosity [e.g., *Neuzil*, 1994]. This allows us to assume that the entire pore system of the sediment is available to fluid flow such that the specific surface we measure by methylene blue adsorption represents the surface area exposed to flow, except possibly in the case of the laboratory silica-bentonite mixtures. This assumption may not be fully applicable to lithified mudrocks and shales, since not all of the mineral grain surfaces may be exposed to flow in these rocks, and during the burial process significant recrystallization may occur, particularly in clays [e.g., *Aplin et al.*, 2006; *Day-Stirrat et al.*, 2008]. Further work on very low permeability mudrocks ($k < 10^{-19}$ m^2) is necessary to determine how our technique performs in these lithologies.

7. Conclusions

[43] A newly developed NMR permeability model is valid over a range of lithologies and grain sizes. This model depends on A, the leading coefficient in the widely used SDR equation, which we define in terms of easily measured sediment physical properties. This new technique greatly

increases the utility of NMR measurements for permeability estimation in fine-grained, clay-rich mudstones. Our model is based on equivalence of the SDR equation and the Kozeny permeability model, and requires knowledge of magnetic susceptibility, grain size, specific surface, and porosity. We tested the model against permeability measurements conducted on natural mudstones as well as resedimented mixtures of natural and synthetic material. We found that we can compute permeability accurately ($R^2 = 0.860$) over four orders of magnitude from 10^{-15} to 10^{-19} m^2 for sediments of widely varying specific surface and magnetic susceptibility. The model is validated by its consistency in determining A and permeability for Berea sandstone, which is a rock type for which the conventional SDR equation works well. Accurate permeability estimation using our model requires a few data points to calibrate α and β, which relate magnetic susceptibility to surface relaxivity, but once these parameters are known the model can be applied broadly among samples of similar mineralogy. Our results provide an improved means of accurate permeability estimation from NMR logs in a wide range of sediments that extends far beyond typical reservoir-quality rocks.

Notation

A SDR equation premultiplier, m^2 s^{-2}.
A_v Avogadro's number, mol^{-1}.
A_{MB} Mineral surface area covered by methylene blue molecule, m^2.
a Grain aspect ratio, m m^{-1}.
B Cross-sectional area of permeameter sample, m^2.
C Amplitude of signal received by NMR tool.
D_{50} Median grain size, m.
H Instantaneous height of sample in CRS test, m.
H_0 Initial height of sample in CRS test, m.
k Permeability, m^2.
M_m Molar mass of methylene blue, g mol^{-1}.
N Number of increments in methylene blue test.
ΔP Pressure difference across sample in permeameter test, Pa.
Q Volumetric flow rate, m^3 s^{-1}.
S_a Specific surface, m^2 kg^{-1}.
T_2 Transverse relaxation time, s.
T_{2LM} Geometric mean of transverse relaxation time distribution, s.
t Time, s.
Δu Pressure difference across sample in CRS test, Pa.
V/S Ratio of pore volume to pore surface area, m.
w Width of clay grain, m.
x Mass fraction, kg kg^{-1}.
α, β Constants in χ - ρ_2 relation, m s^{-1}.
$\dot{\varepsilon}$ Strain rate, s^{-1}.
μ_w Viscosity of water, Pa s.
ν Pore cross-section shape factor, m^2 m^{-2}.
ρ_2 Transverse surface relaxivity, m s^{-1}.
ρ_g Grain density, kg m^{-3}.
τ Tortuosity, m m^{-1}.
φ Porosity, m^3 m^{-3}.
χ Magnetic susceptibility, m^3 m^{-3}.

References

Alvarado, R. J., A. Damgaard, P. Hansen, M. Raven, R. Heidler, R. Hoshun, J. Kovats, C. Morriss, D. Rose, and W. Wendt (2003), Nuclear magnetic resonance logging while drilling, *Oilfield Rev.*, *15*(2), 40–51.

Aplin, A. C., I. F. Matenaar, D. F. McCarty, and B. A. van der Pluijm (2006), Influence of mechanical compaction and clay mineral diagenesis on the microfabric and pore-scale properties of deep-water Gulf of Mexico mudstones, *Clays Clay Miner.*, *54*(4), 500–514, doi:10.1346/CCMN.2006.0540411.

ASTM International (2003), Standard test method for particle-size analysis of soils, *D422-63*, West Conshoshocken, Pa.

ASTM International (2004), Standard test methods for measurement of hydraulic conductivity of saturated porous materials using a flexible wall permeameter, *D5084-03*, West Conshoshocken, Pa.

ASTM International (2006), Standard test method for one-dimensional consolidation properties of saturated cohesive soils using controlled-strain loading, *D4186-06*, West Conshoshocken, Pa.

Bachir, C. (2009), The influence of calcination temperature on structure and magnetic properties of pillared clays, Ph.D. thesis, Dep. of Civil Eng., Geo- and Env. Sci., Univ. Fridericiana zu Karlsruhe, Karlsruhe, Germany.

Baker, J. C., P. J. R. Uwins, and I. D. R. Mackinnon (1993), ESEM study of illite/smectite freshwater sensitivity in sandstone reservoirs, *J. Petrol. Sci. Eng.*, *9*(2), 83–94, doi:10.1016/0920-4105(93)90069-Q.

Banavar, J. R., and L. M. Schwartz (1987), Magnetic resonance as a probe of permeability in porous media, *Phys. Rev. Lett.*, *58*(14), 1411–1414, doi:10.1103/PhysRevLett.58.1411.

Bear, J. (1972), *Dynamics of Fluids in Porous Media*, Elsevier, New York.

Bennett, R. H., K. M. Fischer, D. L. Lavoie, W. R. Bryant, and R. Rezak (1989), Porometry and fabric of marine clay and carbonate sediments: Determinants of permeability, *Mar. Geol.*, *89*, 127–152, doi:10.1016/0025-3227(89)90030-3.

Bernabe, Y., and W. F. Brace (1990), Deformation and fracture of Berea sandstone, in *The Brittle-Ductile Transition in Rocks: The Heard Volume*, *Geophys. Monogr. Ser.*, vol. 56, edited by A. G. Duba et al., pp. 91–102, AGU, Washington, D. C.

Blum, P. (1997), Physical properties handbook: A guide to the shipboard measurement of physical properties of deep-sea cores, *ODP Tech. Note 26*, Ocean Drill. Program, College Station, Tex. [Available at http://www-odp.tamu.edu/publications/tnotes/tn26/TOC.HTM.]

Boudreau, B. P., and F. J. R. Meysman (2006), Predicted tortuosity of muds, *Geology*, *34*(8), 693–696, doi:10.1130/G22771.1.

Carman, P. C. (1937), Flow through a granular bed, *Trans. Inst. Chem. Eng.*, *15*, 150–156.

Caruso, L., G. Simmons, and R. Wilkens (1985), The physical properties of a set of sandstones - Part I. The samples, *Int. J. Mech. Min. Sci. Geomech. Abstr.*, *22*(6), 381–392, doi:10.1016/0148-9062(85)90003-8.

Coelho, D., J.-F. Thovert, and P. M. Adler (1997), Geometrical and transport properties of random packings of spheres and aspherical particles, *Phys. Rev. E*, *55*(2), 1959–1978, doi:10.1103/PhysRevE.55.1959.

Costa, A. (2006), Permeability-porosity relationship: A reexamination of the Kozeny-Carman equation based on a fractal pore-space geometry assumption, *Geophys. Res. Lett.*, *33*, L02318, doi:10.1029/2005GL025134.

Dahlin, D. C., and A. R. Rule (1993), *Magnetic Susceptibility of Minerals in High Magnetic Fields*, U.S. Bur. Mines Rep. Invest. 9449, U.S. Gov. Print. Off., Washington, D. C.

Daigle, H., and B. Dugan (2009), Extending NMR data for permeability estimation in fine-grained sediments, *Mar. Pet. Geol.*, *26*(8), 1419–1427, doi:10.1016/j.marpetgeo.2009.02.008.

Dashen, R., P. Day, W. Kenyon, C. Straley, and J. Willemsen (1987), T1-permeability correlations, *AIP Conf. Proc.*, *154*, 37–62, doi:10.1063/1.36384.

Day-Stirrat, R. J., A. C. Aplin, J. Środoń, and B. A. van der Pluijm (2008), Diagenetic reorientation of phyllosilicate minerals in paleogene mudstones of the Podhale Basin, southern Poland, *Clays Clay Miner.*, *56*(1), 100–111, doi:10.1346/CCMN.2008.0560109.

Dugan, B. (2008), Fluid flow in the Keathley Canyon 151 mini-basin, northern Gulf of Mexico, *Mar. Pet. Geol.*, 25(9), 919–923, doi:10.1016/j.marpetgeo.2007.12.005.

Dugan, B., and H. Daigle (2011), Data report: Permeability, compressibility, stress state, and grain-size of shallow sediments from the sites C0004, C0006, C0007, and C0008 of the Nankai accretionary complex, *Proc. Integr. Ocean Drill. Program*, 314/315/316, 11 pp., doi:10.2204/iodp.proc.314315316.208.2011.

Expedition 308 Scientists (2006), Methods, *Proc. Proc. Integr. Ocean Drill. Program*, 308, 44 pp., doi:10.2204/iodp.proc.308.102.2006.

Expedition 316 Scientists (2009), Expedition 316 methods, *Proc. Integr. Ocean Drill. Program*, 314/315/316, doi:10.2204/iodp.proc.314315316.132.2009.

Flemings, P. B., et al. (2006), Expedition 308 summary, *Proc. Integr. Ocean Drill. Program*, 308, 70 pp., doi:10.2204/iodp.proc.308.101.2006.

Happel, J., and H. Brenner (1983), *Low Reynolds Number Hydrodynamics With Special Applications to Particulate Media*, Martins Nijhoff, The Hague, Netherlands.

Hiltl, M., C. R. Hagelberg, R. P. Swift, T. C. Carney, and W. J. Nellis (1999), Dynamic response of Berea Sandstone shock loaded under dry, wet, and water-pressurized conditions, paper presented at International Conference on High Pressure Science and Technology, Int. Assoc. for Adv. High Pressure Sci. and Tech., Honolulu.

Huang, C.-C. (1997), Estimation of rock properties by NMR relaxation methods, M.S. thesis, Dep. of Chem. Eng., Rice Univ., Houston, Tex.

Hürlimann, M. D. (1998), Effective gradients in porous media due to susceptibility differences, *J. Magn. Reson.*, 131, 232–240, doi:10.1006/jmre.1998.1364.

Hutchinson, D. R., P. E. Hart, T. S. Collett, K. M. Edwards, D. C. Twichell, and F. Snyder (2008), Geologic framework of the 2005 Keathley Canyon gas hydrate research well, northern Gulf of Mexico, *Mar. Pet. Geol.*, 25(9), 906–918, doi:10.1016/j.marpetgeo.2008.01.012.

John, C. M., and T. Adatte (2009), Data report: X-ray analyses of bulk sediment in IODP Holes U1320A and U1324B, northern Gulf of Mexico, *Proc. Integr. Ocean Drill. Program*, 308, 19 pp., doi:10.2204/iodp.proc.308.214.2009.

Kenyon, W. E., and J. A. Kolleeny (1995), NMR surface relaxivity of calcite with adsorbed Mn^{2+}, *J. Colloid Interface Sci.*, 170(2), 502–514, doi:10.1006/jcis.1995.1129.

Kenyon, W. E., P. I. Day, C. Straley, and J. F. Willemsen (1988), A three-part study of NMR longitudinal relaxation properties of water-saturated sandstones, *SPE Form. Eval.*, 3(3), 622–636, doi:10.2118/15643-PA.

Kenyon, W. E., R. L. Kleinberg, C. Straley, G. Gubelin, and C. Morriss (1995), Nuclear magnetic resonance imaging—Technology for the 21st century, *Oilfield Rev.*, 7(3), 19–33.

Kleinberg, R. L. (1996), Utility of NMR T_2 distributions, connection with capillary pressure, clay effect, and determination of the surface relaxivity parameter ρ_2, *Magn. Reson. Imaging*, 14(7–8), 761–767, doi:10.1016/S0730-725X(96)00161-0.

Kleinberg, R. L. (1999), Nuclear magnetic resonance, in *Methods in the Physics of Porous Media*, edited by P.-Z. Wong, pp. 337–385, Academic, San Diego, Calif.

Kleinberg, R. L., C. Flaum, C. Straley, P. G. Brewer, G. E. Malby, E. T. Peltzer III, G. Friedrich, and J. P. Yesinowski (2003), Seafloor nuclear magnetic resonance assay of methane hydrate in sediment and rock, *J. Geophys. Res.*, 108(B3), 2137, doi:10.1029/2001JB000919.

Kozeny, J. (1927), Über kapillare Leitung des Wassers im Boden-Aufstieg, Versickerung und Anwendung auf die Bewässerung, *Sitz. Akad. Wiss. Wien*, 136, 271–306.

Lide, D. R. (Ed.) (2009), *Handbook of Chemistry and Physics*, 90th ed., Chem. Rubber Co., Cleveland, Ohio.

Martys, N. S., S. Torquato, and D. P. Bentz (1994), Universal scaling of fluid permeability for sphere packings, *Phys. Rev. E*, 50(1), 403–408, doi:10.1103/PhysRevE.50.403.

Matteson, A., J. P. Tomanic, M. M. Herron, D. F. Allen, and W. E. Kenyon (2000), NMR relaxation of clay/brine mixtures, *SPE Reservoir Eval. Eng.*, 3(5), 408–413.

Mazzei, D. P. C. (2008), Normalized mechanical properties of resedimented Gulf of Mexico clay from Integrated Ocean Drilling Program Expedition Leg 308, M.S. thesis, Dep. of Civ. and Env. Eng., Mass. Inst. of Tech., Cambridge.

Menéndez, B., W. Zhu, and T.-F. Wong (1996), Micromechanics of brittle faulting and cataclastic flow in Berea sandstone, *J. Struct. Geol.*, 18(1), 1–16, doi:10.1016/0191-8141(95)00076-P.

Neuzil, C. (1994), How permeable are clays and shales?, *Water Resour. Res.*, 30, 145–150, doi:10.1029/93WR02930.

Panda, M. N., and L. W. Lake (1994), Estimation of single-phase permeability from parameters of particle-size distribution, *AAPG Bull.*, 78(7), 1028–1039.

Paterson, L., S. Painter, M. A. Knackstedt, and W. V. Pinczewski (1996), Patterns of fluid flow in naturally heterogeneous rocks, *Physica A*, 233, 619–628, doi:10.1016/S0378-4371(96)00199-9.

Peyron, M., G. K. Pierens, A. J. Lucas, L. D. Hall, and R. C. Stewart (1996), The modified stretched-exponential model for characterization of NMR relaxation in porous media, *J. Magn. Reson., Ser. A*, 118, 214–220.

Santamarina, J. C., K. A. Klein, and M. A. Fam (2001), *Soils and Waves*, John Wiley, Chichester, U. K.

Santamarina, J. C., K. A. Klein, Y. H. Wang, and E. Prencke (2002), Specific surface: Determination and relevance, *Can. Geotech. J.*, 39, 233–241, doi:10.1139/t01-077.

Sawyer, D. E., R. Jacoby, P. B. Flemings, and J. T. Germaine (2009), Data report: Particle size analysis of sediments in the Ursa Basin, IODP Expedition 308 Sites U1324 and U1322, northern Gulf of Mexico, *Proc. Integr. Ocean Drill. Program*, 308, 20 pp., doi:10.2204/iodp.proc.308.205.2008.

Sayers, C. M., J. G. van Munster, and M. S. King (1990), Stress-induced ultrasonic anisotropy in Berea sandstone, *Int. J. Mech. Min. Sci. Geomech. Abstr.*, 27(5), 429–436, doi:10.1016/0148-9062(90)92715-Q.

Scheidegger, A. (1974), *The Physics of Flow Through Porous Media*, 3rd ed., Univ. of Toronto Press, Toronto, Ontario, Canada.

Schreiner, W. H., K. C. Lombardi, A. J. A. de Oliveira, N. Mattoso, M. Abbate, F. Wypych, and A. S. Mangrich (2002), Paramagnetic anisotropy of a natural kaolinite and its modification by chemical reduction, *J. Magn. Magn. Mater.*, 241(2–3), 422–429, doi:10.1016/S0304-8853(01)00480-2.

Schultheiss, P., M. Holland, and J. Roberts (2006), Gulf of Mexico Gas Hydrates Joint Industry Project pressure coring and core logging, in *Cruise Report: The Gulf of Mexico Gas Hydrate Joint Industry Project*, edited by G. E. Claypool, 54 pp., Nat. Energy Tech. Lab., Morgantown, W. Va. [Available at http://www.netl.doe.gov/technologies/oil-gas/publications/Hydrates/reports/GOMJIPCruise05.pdf.]

Schwartz, L. M., and J. R. Banavar (1989), Transport properties of disordered continuum systems, *Phys. Rev. B*, 39(16), 11965–11971, doi:10.1103/PhysRevB.39.11965.

Screaton, E. J., et al. (2009), Expedition 316 summary, *Proc. Integr. Ocean Drill. Program*, 314/315/316, 29 pp., doi:10.2204/iodp.proc.314315316.131.2009.

Seevers, D. O. (1966), A nuclear magnetic method for determining the permeability of sandstones, paper presented at 7th Annual Logging Symposium, Soc. Petrophys. Well Log Anal., Tulsa, Okla.

Serra, O. (1990), *Element Mineral Rock Catalog*, Schlumberger Ltd., Sugar Land, Tex.

Slade, P. G., J. P. Quirk, and K. Norrish (1991), Crystalline swelling of smectite samples in concentrated NaCl solutions in relation to layer charge, *Clays Clay Miner.*, 39(3), 234–238, doi:10.1346/CCMN.1991.0390302.

Straley, C., D. Rossini, H. Vinegar, P. Tutunjian, and C. Morriss (1994), Core analysis by low field NMR, paper presented at 1994 International Symposium, Soc. Core Anal., Stavanger, Norway.

Velde, B. (1996), Compaction trends of clay-rich deep sea sediments, *Mar. Geol.*, 133, 193–201, doi:10.1016/0025-3227(96)00020-5.

Watson, A. T., and C. T. P. Chang (1997), Characterizing porous media with NMR methods, *Prog. Nucl. Magn. Reson. Spectrosc.*, 31, 343–386, doi:10.1016/S0079-6565(97)00053-8.

Winters, W. J., B. Dugan, and T. S. Collett (2008), Physical properties of sediments from Keathley Canyon and Atwater Valley, JIP Gulf of Mexico gas hydrate drilling program, *Mar. Pet. Geol.*, 25(9), 896–905, doi:10.1016/j.marpetgeo.2008.01.018.

Wong, R. C. K. (2003), A model for strain-induced permeability anisotropy in deformable granular media, *Can. Geotech. J.*, 40, 95–106, doi:10.1139/t02-088.

Xu, P., and B. Yu (2008), Developing a new form of permeability and Kozeny-Carman constant for homogeneous porous media by means of fractal geometry, *Adv. Water Resour.*, 31, 74–81, doi:10.1016/j.advwatres.2007.06.003.

Yang, Y., and A. C. Aplin (1998), Influence of lithology and compaction on the pore size distribution and modelled permeability of some mudstones from the Norwegian margin, *Mar. Pet. Geol.*, 15, 163–175, doi:10.1016/S0264-8172(98)00008-7.

Yang, Y., and A. C. Aplin (2007), Permeability and petrophysical properties of 30 natural mudstones, *J. Geophys. Res.*, 112, B03206, doi:10.1029/2005JB004243.

Yang, Y., and A. C. Aplin (2010), A permeability-porosity relationship for mudstones, *Mar. Pet. Geol.*, 27, 1692–1697, doi:10.1016/j.marpetgeo.2009.07.001.

Yun, T. S., G. A. Narsilio, and J. C. Santamarina (2006), Physical characterization of core samples recovered from Gulf of Mexico, *Mar. Pet. Geol.*, 23, 893–900, doi:10.1016/j.marpetgeo.2006.08.002.

Zhang, Q. (2001), NMR formation evaluation: Hydrogen index, wettability and internal field gradients, Ph.D. thesis, Dep. of Chem. Eng., Rice Univ., Houston, Tex.

Zhang, X., and M. A. Knackstedt (1995), Direct simulation of electrical and hydraulic tortuosity in porous solids, *Geophys. Res. Lett.*, 22(17), 2333–2336, doi:10.1029/95GL02230.

H. Daigle and B. Dugan, Department of Earth Science, Rice University, 6100 Main St., MS-126, Houston, TX 77005, USA. (hcd1@rice.edu; dugan@rice.edu)